Laser Photonics Rev. **5**, No. 4, 479–495 (2011) / **DOI** 10.1002/lpor.201000017

LASER & PHOTONICS REVIEWS

Abstract Recent progress in the field of re-locatable photonic crystal resonators is discussed with a particular emphasis on the flexible scheme that employs highly-curved microfiber. In this scheme a spectrally-tunable high-quality-factor resonator can be defined repeatedly by physically moving a curved microfiber to a new position. When a curved microfiber is placed on top of a photonic crystal waveguide (or photonic crystal), a photonic well is newly created in the vicinity of the contact point. Inside of this photonic well, high-quality-factor resonant modes are generated at frequencies below the cutoff edge of the guided mode. The tapered microfiber is an integral part of a single mode optical fiber and efficient out-coupling is naturally obtained. The sub-nanometer spectral tuning capability that is available by changing the curvature of the microfiber is also an important characteristic and discussed. This spectrally- and spatially-reconfigurable photonic crystal resonator is expected to be a potential platform for photonic crystal based single photon sources, which enables accurate spatial overlap and spectral overlap with a single quantum dot, together with straightforward photon out-coupling to the fiber with high efficiency.

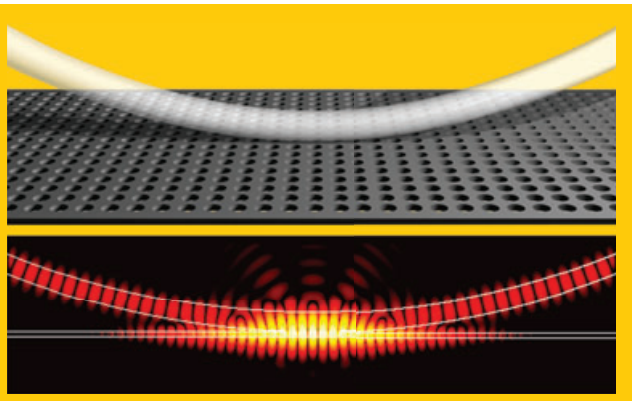

On-demand photonic crystal resonators

Myung-Ki Kim[1,2], Ju-Young Kim[1], Ju-Hyung Kang[1], Byeong-Hyeon Ahn[1], and Yong-Hee Lee[1,3,*]

1. Ex-situ trimming of resonant cavity

In recent years, the field of photonic crystal research has been moving forward at a pace exceeding our expectation and is reaching (or already in) the stage of maturity and engineering. Now, in midst of this development and interest, various applications based on photonic crystals (PhCs) have been proposed. Functional photonic waveguides [1–5], high-quality-factor photonic crystal resonators and lasers [6–15], photonic crystal LEDs [16–20], and photonic integrated circuits [21–24] are a few examples of these efforts. Among these devices, the photonic crystal resonator has been drawing attentions of researchers working in various fields of different disciplines. The wavelength-scale photonic crystal resonator can function as a discrete single device or as an essential component of a certain photonic integrated circuit.

In practice, the spectral position of a resonance in the fabricated high-Q resonator usually deviates, on the order of a nanometer, from the intended target value. Sometimes an extremely large number of cavities are fabricated at once, in the hope that one can find more than one useful devices. Post trimming of the cavity, therefore, has been in great demand and so multitudes of special post-tuning methods have been proposed and tested. However, the accurate control of the wavelength-scale cavity is nontrivial in both spectral and spatial domains. Most of the spectral cavity tuning methods can be classified into two categories according to the physics of perturbation. The first category relies on the control of the material property (refractive index) [25–29], and the other is the geometric or physical perturbation of resonators [30–33]. Several methods based on the control of the refractive index have been demonstrated. Note that the upper bound of the available index change is on the order of $10^{-4} \sim 10^{-3}$ and one can expect the relative spectral shift of similar magnitude. M. W. Lee et al. reported photosensitive post-tuning techniques using chalcogenide glass in order to tune the dispersion of a PhC waveguide [25]. The same group used the photosensitive property of the chalcogenide to write a high Q cavity and tune the resonant wavelength of this cavity [29]. They observed large index change (Δn) of 0.03 in the exposed region.The index tuning method utilizing thermo-optic effects has also been reported [26–28]. By integrating thin film heater with a microcavity, resonance shift of $\sim$ 5 nm was achieved with 1.2-mA current injection [26].

Various geometric deformation/perturbation techniques have also been investigated. In 2005 A. Badolato et al. demonstrated deterministic approaches applicable to solid-state cavity quantum electrodynamics (QEDs). Their digital etching techniques enabled both spectral overlap and spatial overlap between a single quantum-dot and a photonic crystal resonator [30]. Here the monolayer-thick oxide layer on GaAs surface was chemically peeled off during each wet etching step [31]. They were able to fabricate high-Q cavities ($Q > 5{,}000$) that red-shifted by 13 nm with respect to the quantum dot resonance. Physical deformation methods have also been suggested. W. Park et al. studied photonic crystal structures under mechanical stresses by employing a microelectromechanical system (MEMS) [32]. This tech-

[1] Department of Physics, KAIST, Daejeon 305-701, Korea [2] Department of Electrical Engineering and Computer Sciences, University of California, Berkeley, CA 94720, USA [3] Graduate School of Nanoscience and Technology (WCU), KAIST, Daejeon 305-701, Korea
[*] Corresponding author: e-mail: pcvcsel@gmail.com, yhlee@kaist.ac.kr

nique is meaningful in the sense that it provides real-time and dynamic control of photonic crystal band structures. In addition, the infiltration of high-index liquid to air-holes of photonic crystals has been proposed and tested. In 1999, liquid crystals were suggested as means to tune static properties of photonic crystal structures [34]. And, in 2003 and 2004, the large index change ($\Delta n \approx 0.05$) of the liquid crystal enabled the wide spectral tuning, through electrical [35] and thermal [36] effects. Recently, the integration with microfluidics and the perturbation with a tapered fiber and a fiber tip on photonic crystal structures have also been reported [29, 33, 37–42]. Comparison with various post trimming techniques for the fabricated cavity was summarized extensively in the previous LPR article by Grillet et al. [40].

In comparison, for spatial tuning (relocation), there have been limited trials until the recent report utilizing fluid infiltration [38, 43]. The main idea in these references is the formation of photonic crystal double-heterostructure cavities [7] by selective microfluidic infiltration. Here, the position and length of a microfluidic cavity were defined by adjusting the region of infiltration in steps of several microns. Reconfigurability was obtained by immersing the device in toluene. However, repeated cavity relocation was rather slow and awkward. In fact, if one wishes to position a high-Q cavity at an arbitrary point, finding means to re-construct a cavity in an endlessly repeatable fashion becomes important. However, the photonic crystal cavity that is both spectrally- and spatially-tunable is nontrivial to design and yet to be demonstrated. If a truly reconfigurable resonant cavity can be formed at any position on demand, one can envision multitudes of new applications, especially in the field of cavity quantum electrodynamics where high-Q cavity plays a critical role [31].

In this review, recent progress [44, 45] in the spatially- and spectrally-reconfigurable photonic crystal resonator is reviewed with a particular emphasis on the scheme that employs a highly-curved microfiber. In Sect. 2, dispersion characteristics of a photonic crystal waveguide (or a bare photonic crystal) in the presence of a straight microfiber are discussed. Variation of the cutoff frequency of the induced photonic crystal waveguide mode is explained in detail. In Sect. 3, the generic configuration in which a highly-curved microfiber is coupled with a photonic crystal waveguide (or a bare photonic crystal) is explained. The formation of a photonic well and the resultant photon confinement are discussed. The Gaussian-shaped photonic well is formed at a spectral position slightly below the cutoff of the photonic crystal waveguide mode. The position of this resonant cavity can be defined repeatedly by simply relocating a curved microfiber along the photonic crystal waveguide (or the photonic crystal). In Sect. 4, the creation and annihilation of the spatially-reconfigurable photonic crystal resonator is confirmed by the experimental observation of new laser modes. Characteristics of the reconfigurable photonic crystal modes are discussed using the photoluminescence spectra and transmission spectra. In Sect. 5, the direct and efficient photon transfer into external optics through a single-mode fiber is discussed. The out-coupling strength can be controlled by changing the curvature of the microfiber or the fine structural modification of the photonic crystal parameters. In Sect. 6, the spectral tuning capability of the reconfigurable photonic crystal cavity is discussed. In Sect. 7, the prospect of the spatially- and spectrally-reconfigurable resonator is summarized.

2. Microfiber-induced photonic crystal waveguide

2.1. Triangular photonic crystal waveguide and straight microfiber

Consider a two-dimensional triangular-lattice photonic crystal slab W1-waveguide as a host structure. In general one of the most straightforward tools of understanding the photonic crystal waveguide is the dispersion curve. In the two-dimensional (2-D) slab photonic crystal structure, the slab thickness is chosen to be less than a half of operating wavelength such that it allows only one guided mode in the slab. This simple $\lambda/2$ slab configuration simplifies subsequent theoretical analyses and, therefore, is widely employed.

Now let's place a straight microfiber on top of the waveguide as shown in Fig. 1a and look for the resultant perturbation by inspecting the modified dispersion curve. Usually the effective index of a guided mode is determined by the dielectric media interacting with the slab through evanescent coupling. When the straight silica microfiber (instead of air) is placed on top of the 2-D slab photonic crystal waveguide (Fig. 1a), the dispersion curve shifts slightly downward in frequency as shown in Fig. 1c. For better understanding of underlying physics, the intensity profile of the guided mode with fiber is plotted in Fig. 1b. One can see the asymmetric photon distribution originating from the presence of the fiber. Note that evanescent fields penetrate more deeply into the fiber (SiO_2) region than the air side. The photonic crystal waveguide mode feels the existence of the upper microfiber through the evanescent field. The net effect shows up as the increase of effective index of the guided mode [46]. One can easily see this effect by changing the air gap between the waveguide and the microfiber as shown in Fig. 1c. The cutoff frequency (wavelength) of the guided mode decreases (increases) with the air gap size. Through the 3-dimensional finite difference time domain (FDTD) computation, we find that the shift of the cutoff frequency $\delta\omega_{\text{cutoff}}$ has an exponential dependence on the air-gap, as shown in Fig. 1d and can be represented by the simple functional form.

$$\delta\omega_{\text{cutoff}} \propto -\delta\varepsilon_{\text{eff}} \propto -e^{-d/\alpha}. \qquad (1)$$

Here, ω_{cutoff} and ε_{eff} represent the cutoff frequency and the effective dielectric constant, respectively. d and α denote an air-gap and the decay length, respectively. In the model shown in Fig. 1, the decay length α is calculated to be 62.5 nm where the slab thickness and the radius of period air-holes are fixed at 200 nm and $0.30a$, respectively. Here a is the lattice constant. The diameter of the microfiber is chosen to be 1.0 μm such that only single fiber-mode, LP_{01} mode [47], is allowed.

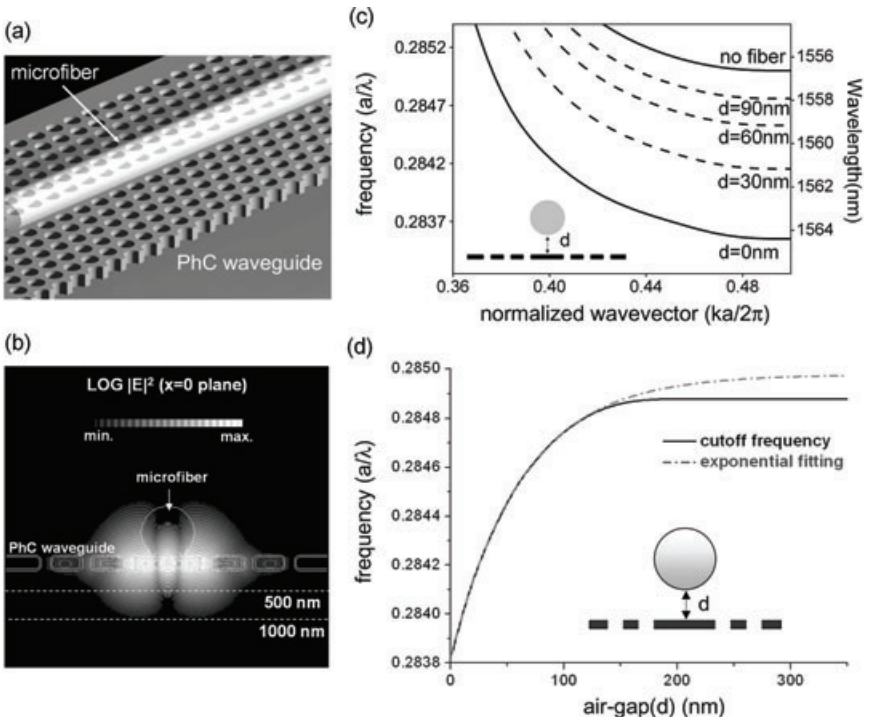

Figure 1 (a) Photonic crystal slab waveguide with straight microfiber. (b) Electric field intensity profile showing evanescent field of guided mode. (c) Dispersion characteristics of photonic crystal waveguide with straight microfiber held at different heights. (d) Cutoff frequency variation as function of air gap. Gray dash-dotted line represents the best exponential fit curve.

Variation of the cutoff frequency as a function of the gap is summarized in Fig. 1d where the dotted line is an exponential function that fits best to the FDTD results. These two curves seem to agree well when the air-gap is less than 150 nm. However, for the air gap >150 nm, the agreement is worse because the evanescent field does not cover the region of the microfiber faithfully, as shown in Fig. 1b.

2.2. Square-lattice photonic crystal with straight microfiber

Now consider a straight microfiber placed on top of a bare square-lattice photonic crystal slab (with no waveguide) and find out whether new microfiber-induced waveguide modes can be generated again as in Sect. 2.1. New effects introduced by the presence of a straight fiber on top of the square-lattice photonic crystal slab are studied by FDTD analyses as shown in Fig. 2. Square lattice of air holes are drawn on a 200-nm-thick slab (n=3.4) with a periodicity (a) of 500 nm. The radius (r) of the air hole is $0.35a$. The diameter of the microfiber is 1.0 µm.

Here it is important to align the straight microfiber along the Γ-X direction of the square lattice photonic crystal. The Γ-X direction is the nearest-neighbor direction of the square lattice. Formation of guided modes along the other direction is unlikely because the light cone folding deteriorates the photonic band gap characteristics [48]. The case of the triangular photonic crystal is also tested and found to be not suitable for the generation of the resonant cavity. TE-like resonant cavity modes are found to be excessively lossy because of the coupling with TM-like guided modes. This TE-TM coupling stems from the broken symmetry in the presence of silica fiber on one side of the slab. In comparison, in the case of the square-lattice photonic crystal, the fiber-induced resonant modes along the Γ-X direction experiences much smaller TE-TM coupling losses and could have high-Q factors.

Figure 2a shows the dispersion of the microfiber-induced waveguide modes of different contact alignments ($s = 0.0 \sim 0.5a$). The shift parameter (s) is defined such that s equals $0.0a$ when the fiber is placed right above the centers of the air holes and s equals $0.5a$ when the fiber is placed between the air holes. Note that new waveguide modes are created inside the photonic bandgap. The electric field (E_y) profile of a waveguide-mode at the dispersion edge ($k_n = 0.5$) is plotted in the inset of Fig. 2a for the case of $s = 0.5a$. Various contact situations are investigated in order to confirm the formation of the new waveguide, as shown in Fig. 2b and (c). In the induced-waveguide mode, the photon energy is concentrated mainly in the photonic crystal slab beneath the straight-microfiber. The six dispersion curves in Fig. 2a look almost like one under current experimental conditions where the fiber size is larger than the lattice constant and almost the same amount of photon energy resides in the photonic crystal slab, independent of the shift (s).

Note that the newly-generated induced-waveguide mode has a cutoff frequency below which no propagating mode is allowed. Figure 2d shows the cutoff frequency variation as a function of air gap size. The cutoff frequency decreases as the microfiber comes closer to the slab due to the increased effective index. The cutoff frequency of the microfiber-induced waveguide falls off from $\omega_n = 0.3348$ (the band edge frequency of the photonic crystal slab) and decreases down to the minimum, $\omega_n = 0.3293$, when the microfiber is in contact with the slab. The spectral separation ($\Delta\omega$) between the cut-off frequencies with and without

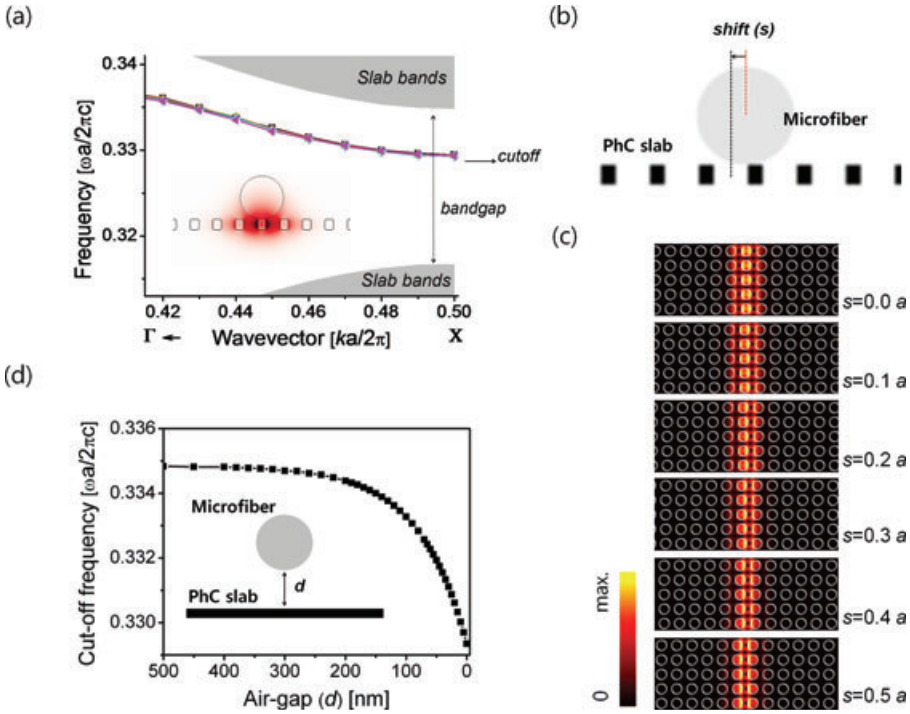

Figure 2 (online color at: www.lpr-journal.org) Formation of waveguide modes in square lattice photonic crystal (PhC) slab. (a) Dispersion curves of microfiber-induced waveguide modes. Six curves of different shifts (s) are drawn simultaneously. The inset is the E_y pattern at the band edge and $s = 0.5a$. (b) Cross-section of the straight-microfiber in contact with photonic crystal slab. (c) Horizontal cross sections of electric field intensity distribution at $k_n = 0.5$. (d) Cutoff frequency of induced guided modes as a function of the air gap.

fiber is 0.0055, equivalent to $\Delta\lambda = 24.9$ nm at a wavelength of 1.5 µm. It is worth pointing out that this spectral shift of the induced-waveguide is almost an order of magnitude larger than that of the previous fiber-coupled photonic crystal waveguide. This is understandable by comparing the relative sizes of the perturbations introduced by the presence of the microfiber: the effective index of the photonic crystal waveguide mode is larger than that of the bare photonic crystal slab mode.

3. Curved microfiber in contact with photonic crystal: 'photonic' well

3.1. Photonic well formed in photonic crystal waveguide

The situation becomes interesting when a highly-curved microfiber is placed on top of the waveguide. In this situation, the air gap d has a quadratic dependence on the x coordinate along the triangular photonic crystal waveguide and the cutoff frequency shift $\delta\omega_{\text{cutoff}}$ can be expressed as follows.

$$\delta\omega_{\text{cutoff}} \propto -e^{-d/\alpha} = -e^{-x^2/2R\cdot\alpha} \qquad (2)$$

Here R is the radius of curvature of the microfiber, and x is the coordinate of the direction of the photonic crystal waveguide. Here the contour of the cutoff frequency shift $\delta\omega_{\text{cutoff}}$ generates a Gaussian profile as a function of the coordinate x, as shown in Fig. 3. The Gaussian dependence of $\delta\omega_{\text{cutoff}}$ stems from the exponentially-decaying evanescent field, having an exponent proportional to d/α. The dotted-line in Fig. 3 represents the Gaussian fit curve of the cutoff frequencies computed by the FDTD method.

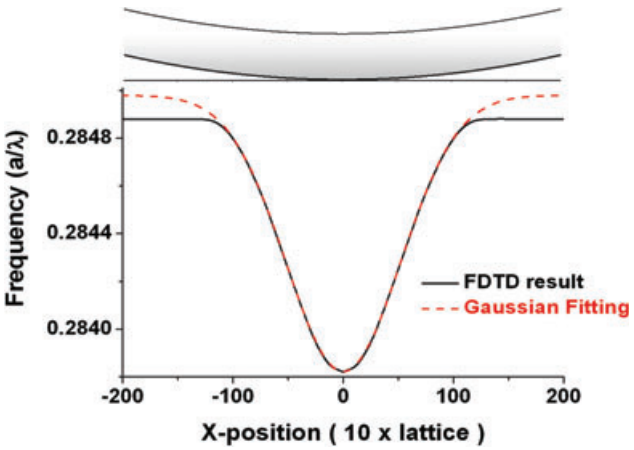

Figure 3 (online color at: www.lpr-journal.org) Gaussian-shaped photonic well following the cutoff frequency profile. The radius of curvature of the microfiber is 70 µm. Dashed line represents a Gaussian fit.

In fact, the situation becomes interesting in the spectral vicinity of the band edge. For example, the cutoff frequency of the TE1-even guided mode moves downwards upon the contact of the curved microfiber [46]. A modified cutoff frequency profile is newly formed inside the photonic band gap where no propagating mode exists. This spectrally-localized cutoff frequency contour inside the photonic band gap can be viewed as a 'photonic' well that can confine photons inside a wavelength-scale volume. This photonic well is reminiscent of the textbook 1-D quantum mechanical harmonic potential well. In a sense, the underlying physics of the cavity formation is identical to that employed for the double-heterostructure photonic crystal cavity where the

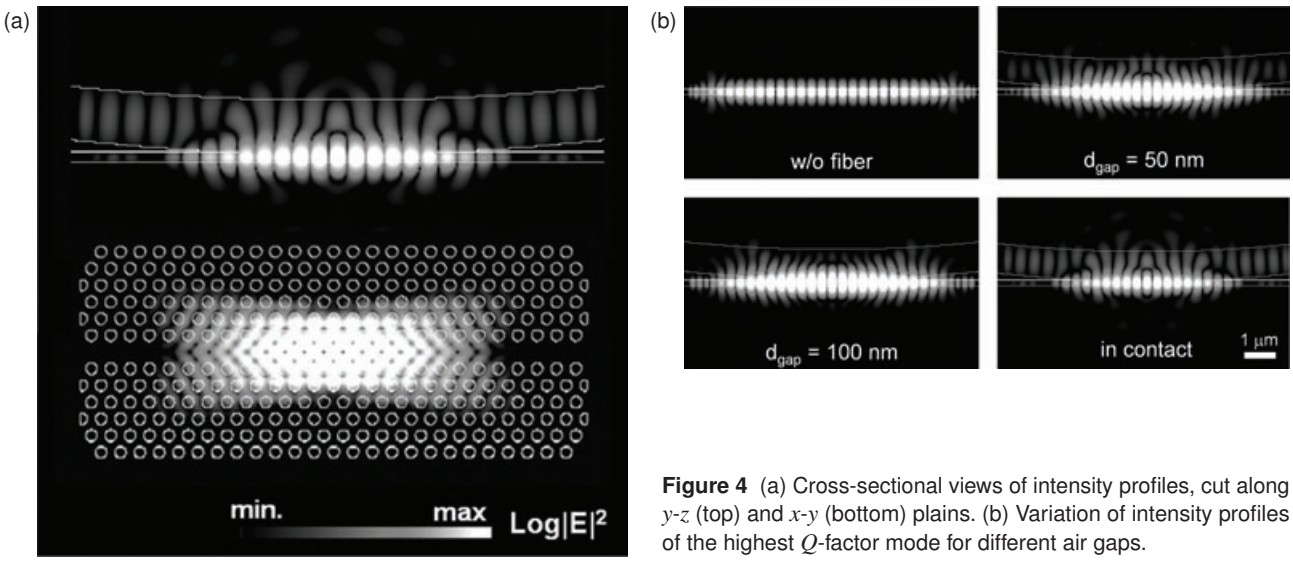

Figure 4 (a) Cross-sectional views of intensity profiles, cut along *y*-*z* (top) and *x*-*y* (bottom) plains. (b) Variation of intensity profiles of the highest *Q*-factor mode for different air gaps.

cutoff frequency is controlled through a fine change of lattice constant [7], a deposition of high-index material [49], or a local index modulation using the photosensitivity of chalcogenide [33] and fluidic infiltration [43].

The next step is the search of new resonant modes that could possibly be contained in the photonic well. The identification of new resonant modes can be one way of claiming the creation of a new photonic crystal cavity. In this novel configuration, the position of the reconfigurable photonic crystal cavity (RPC) can be defined and re-defined, by simple moving the physical position of the curved microfiber. In the computational analyses shown in Fig. 4, the curved microfiber has a radius of curvature of 70 μm. And the slab thickness and the radius of air-holes are fixed at 200 nm and 0.30*a*, respectively. In order to witness the birth of the new resonant mode in the photonic well, the intensity profile of the highest *Q*-factor mode along the waveguide is plotted in Fig. 4b, as one moves the curved microfiber toward the surface of the photonic crystal waveguide. Observe that photons become more tightly localized in case of the smaller air gap.

When the fiber is in complete contact, the deepest photonic well is formed and the *Q*-factor of the fundamental RPC mode is found to be the largest. The maximum *Q*-factor of 1,300,000 is found at a normalized frequency of 0.2839 with a coupling efficiency (η) of 26%. In comparison, when the fiber is not in complete contact (air-gap=100 nm), the *Q*-factor of the corresponding shallow RPC mode decreases to 170,000 with coupling efficiency $<1\%$. The frequency separation between this RPC resonance and the waveguide cutoff is 0.0011, equivalent to $\Delta\lambda = 5.8$ nm. The mode volume is $2.6(\lambda/n)^3$. In fact, a total of three resonant modes exist in the Gaussian photonic potential well (Fig. 5). *Q*-factors of the second and the third mode are 3.2×10^5 and 1.8×10^5, respectively, smaller than that of the fundamental mode. The mode-volumes are $3.2(\lambda/n)^3$ and $3.9(\lambda/n)^3$ with resonant frequencies of 0.2842 and 0.2845, respectively. Note that the fundamental RPC mode is located at the bottom region in the photonic well with $R = 70\,\mu$m, $\alpha = 62.5$ nm and $\delta\omega_{\max} = 0.0011$.

In general, the shapes of Gaussian and parabolic function are almost indistinguishable near the bottom. With this

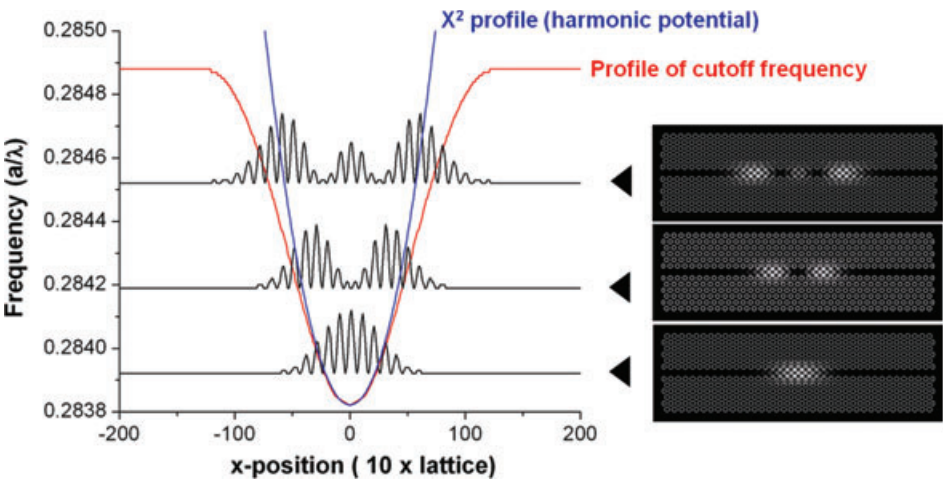

Figure 5 (online color at: www.lpr-journal.org) New modes found in Gaussian photonic potential well by 3D FDTD computations. Right figures show the intensity profiles of the corresponding modes.

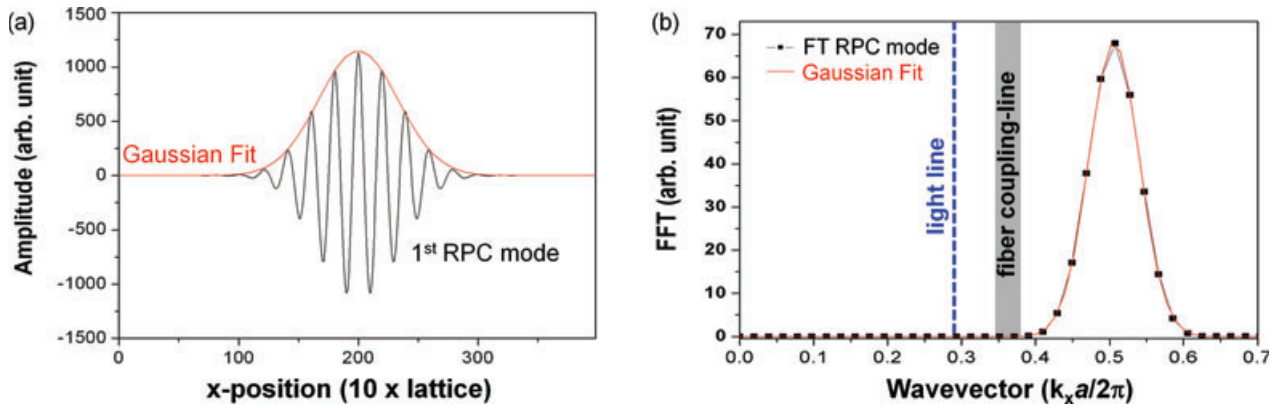

Figure 6 (online color at: www.lpr-journal.org) (a) Electric field amplitude of the lowest-order 1-D RPC mode. (b) Fourier transform of the RPC mode shown in (a). Thick vertical line represents the magnitude of **k** vector propagating in silica microfiber of 1 micron in diameter (effective index = 1.2).

in mind, the cutoff frequency as a function of the position x along the waveguide axis due to the presence of the curved taper can be approximated as follow,

$$\begin{aligned}\delta\omega_{\text{cutoff}} &= -\delta\omega_{\max}\cdot e^{-x^2/2R\cdot\alpha} \\ &= -\delta\omega_{\max}\cdot\left(1-\frac{1}{2R\cdot\alpha}x^2+\cdots\right) \\ &\simeq -\delta\omega_{\max}\cdot\left(1-\frac{1}{2R\cdot\alpha}x^2\right). \qquad (3)\end{aligned}$$

And it is not unreasonable to expect that the lowest mode of the Gaussian photonic well, similar to that of the Harmonic potential well, is the Gaussian envelopment function with Hermit polynomials [50]. Accordingly, the fundamental mode of the reconfigurable photonic crystal resonator is expected to assume the Gaussian shape. The smoothly-varying Gaussian mode profile is known to be advantageous in minimizing scattering losses by suppressing the radiating k-components inside the light-cone [6]. This fact partly explains the high Q-factor of the fundamental mode exceeding $\sim 10^6$. Figure 6a shows the electric-field amplitude profile of the fundamental mode following a Gaussian curve closely. One can also confirm that the radiating component inside the light-cone is sufficiently separated from the FT RPC mode (to be explained in more detail in Sect. 5) in Fig. 6b.

3.2. Photonic well on photonic crystal slab with no waveguide

Now let's place a highly-curved microfiber on a square-lattice photonic crystal slab, as shown in Fig. 7a. The formation of a photonic well is easily predicted. The cutoff frequency varies spatially along the microfiber as a function of the air gap distance between the slab and the curved microfiber. As explained in Sect. 3.1, the spatial profile of the cutoff frequency follows the Gaussian functional form again, from the quadratic dependence of the air-gap distance and the exponential nature of the evanescent field (dark yellow line in Fig. 7c). This fiber-induced photonic well is much deeper than that formed in the existing photonic crystal waveguide. However, remember that the 2-D photonic well is induced without the assistance of the existing waveguide and photon confinement along y direction (perpendicular to microfiber) is much weaker than that along the waveguide of 1-D counterpart. Relatively speaking, the area of equi-cuttoff-frequency contour of the 2-D photonic well varies

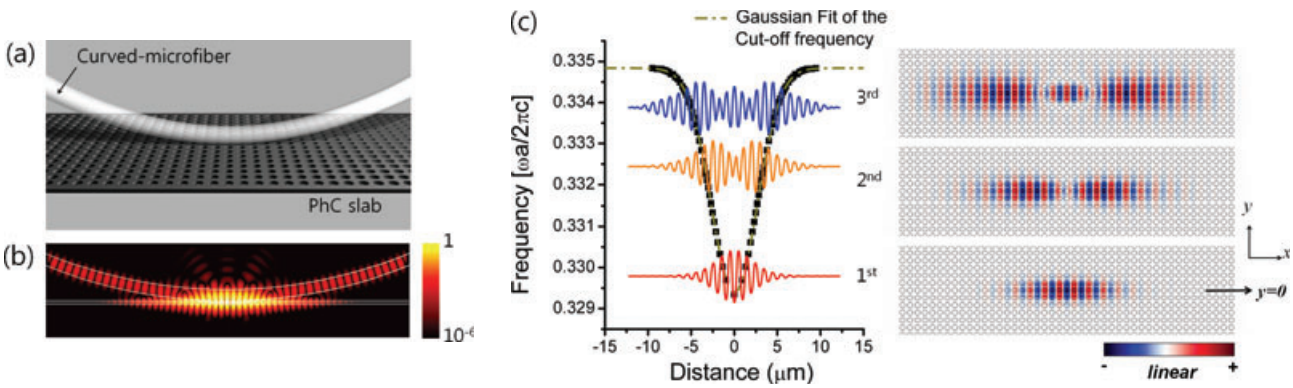

Figure 7 (online color at: www.lpr-journal.org) (a) Schematic of 2-D RPC resonator. (b) Electric field intensity of fundamental RPC mode. (c) Cutoff frequency profile (left) and E_y patterns of 2-D RPC modes at the slab center ($s = 0$) (right).

much more sharply than that of 1-D photonic well and is disadvantageous in supporting many modes. In our analyses, only three resonant modes are identified in this deeper 2-D RPC.

Three RPC resonant modes are identified in the photonic well through FDTD computations. Here the radius of the curvature (R) of the microfiber is set to be $R = 70\,\mu$m. The E_y field profiles of the fundamental RPC mode (1st) and higher-order RPC modes (2nd and 3rd) are shown in the right side of the Fig. 7c. The line graphs of the E_y profiles at the center ($y = 0$) are overlapped with the spatial profile of the cut-off frequency according to their resonant frequencies in order to visualize photon confinement inside the Gaussian photonic well. Red, orange, and blue lines correspond to the 1st, 2nd, and 3rd RPC modes, respectively. The spectral distance between resonant modes are predicted as large as $\Delta\lambda_1$(gap between 1st and 2nd RPC modes) $= 11.3$ nm and $\Delta\lambda_2$(gap between 2nd and 3rd RPC) $= 6.5$ nm. The fundamental (1st) RPC mode has a Q-factor of 25,900 and a high collection efficiency into the microfiber of 80% ($r = 0.35a$). Photons are confined in the proximity of the contact point and evanescently coupled to the microfiber (Fig. 7b). The mode-volume is calculated to be $2.4(\lambda/n)^3$. The Q-factor of the fundamental RPC mode can be further increased up to 2.5×10^5 at the expense of the collection efficiency, by destroying the phase matching conditions between the fiber propagating mode and the fiber-induced resonant mode. For example, the phase matching is adjustable by changing the radius of air-holes. The higher-order RPC modes have smaller Q factors and larger mode volumes than those of the fundamental RPC mode. When $r = 0.35a$, Q-factors of the 2nd and 3rd RPC modes are 3,880 and 1,480 and their mode volumes are $6.0(\lambda/n)^3$ and $9.9(\lambda/n)^3$, respectively.

4. Microfiber-coupled re-locatable photonic crystal cavity

4.1. One-dimensional relocation of resonant cavity

Quaternary semiconductor photonic crystal slab W1-waveguides and highly-curved tapered microfibers (Fig. 8) [47, 51, 52] are fabricated for the experiment. The 200-nm-thick InGaAsP slab contains the InGaAsP four quantum wells in the middle as an active medium emitting near communication wavelength of 1,550 nm. The fabricated PhC InGaAsP slab linear waveguide is 33-μm-long with air-hole radius of $0.30a$. The radius of curvature and the diameter of the microfiber are $\sim 100\,\mu$m and $1.0\,\mu$m, respectively. A 980-nm InGaAs laser diode is used as an optical pump source and fed into one end of the tapered single mode fiber and the photoluminescence spectrum of the reconfigurable resonator is collected from the other end using a wavelength division multiplexing coupler [52] as shown in Fig. 9a.

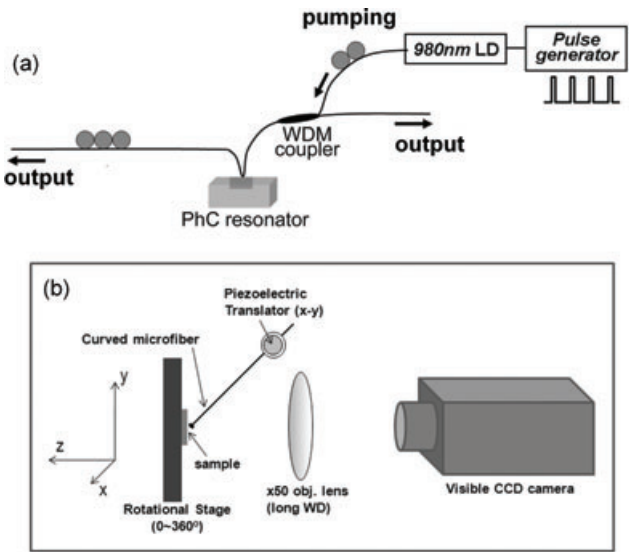

Figure 9 (a) Schematic of experimental setup. (b) Coupling of curved microfiber and photonic crystal resonator.

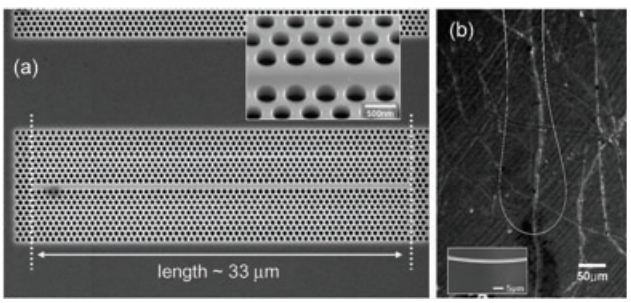

Figure 8 (a) Fabricated photonic crystal slab waveguide. (b) Highly-curved microfiber.

Measured lasing spectra of samples of different lattice constants under the pumping condition which a peak power, a pulse width and a duty cycle are 6.5 mW, 10 ns and 1%, respectively are overlaid in the dispersion diagram obtained by 3-dimensional FDTD methods [53], as shown in Fig. 10. The three lattice constants (418, 460, 512 nm) are chosen to probe three waveguide modes, TE1-like (even), TE1-like (odd) and TE2-like (odd) modes, available for the formation of the RPC resonance. The respective mode profile at the corresponding band edge is plotted in the inset of Fig. 10. Note that all the measured normalized RPC lasing frequencies (0.2913, 0.3119 and 0.3563) are found slightly below the three photonic crystal guided modes, respectively. The peaks other than the RPC modes can also be understood. In fact, the other lasing modes are excited near the band edge where the group velocity is very slow. The Fabry-Perot fringe of the TE1-odd mode ($a = 460$ nm) in Fig. 10 comes from the reflection at the two ends of the finite-length photonic crystal waveguide. The estimated length of the photonic crystal waveguide obtained from the measured fringe spacing ($\Delta\lambda = 8.3$ nm) is 35 μm, in reasonable agreement with the length ($\sim 33\,\mu$m) of the fabricated photonic crystal waveguide. The broad photoluminescence from 0.3130 to 0.3240 is attributed to the flat hill near the center of the

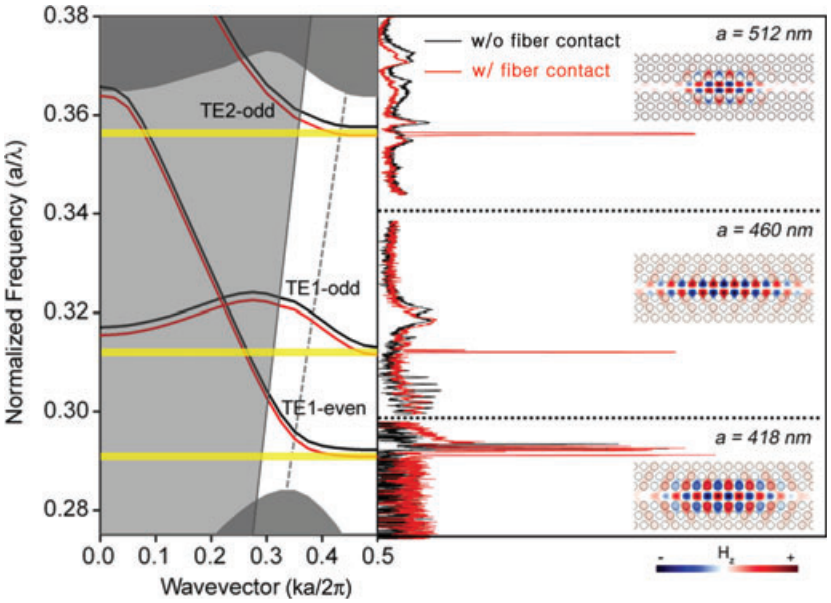

Figure 10 (online color at: www.lpr-journal.org) Measured spectra plotted on top of calculated dispersion curves. Three lattice constants ($a = 512, 460, 418$ nm) correspond to three possible locations available for the formation of 1-D RPC modes. The gray region and the dotted line represent a light-cone and a dispersion of tapered fiber, respectively. On the right-hand side is the vertical magnetic field (H_z) of each RPC mode when a fiber is in contact at the center of waveguide.

TE1-odd mode dispersion curve where the group velocity is small.

For comparison purposes, the reference photoluminescence spectrum that closely represents the bare photonic crystal waveguide is taken while the microfiber is kept ~ 100 nm above the slab, plotted as black lines in Fig. 11. When the air gap size between the microfiber and the photonic crystal waveguide becomes larger than 100 nm, no observable resonant mode is formed. However, the 980-nm pump laser is still able to generate photoluminescent electron-hole pairs in the quantum wells through evanescent pumping. With the microfiber in contact, several reconfigurable photonic crystal modes are newly observed. The red lines of Fig. 11a–c represent photoluminescence spectra when the microfiber is in complete contact with the waveguide.

The 540-nm sample shows a clear single mode lasing at 1604.6 nm (Fig. 11a). In case of the 460-nm sample operat-

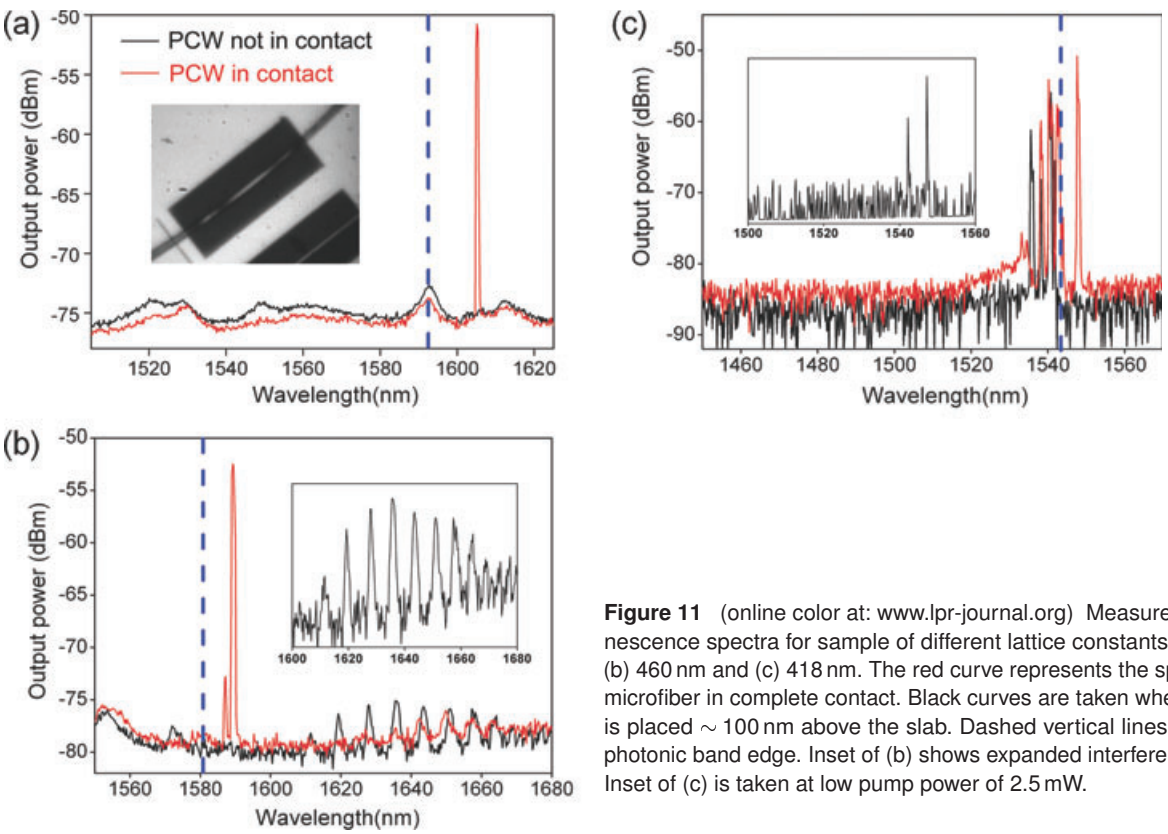

Figure 11 (online color at: www.lpr-journal.org) Measured photoluminescence spectra for sample of different lattice constants: (a) 512 nm, (b) 460 nm and (c) 418 nm. The red curve represents the spectrum with microfiber in complete contact. Black curves are taken when microfiber is placed ~ 100 nm above the slab. Dashed vertical lines indicate the photonic band edge. Inset of (b) shows expanded interference patterns. Inset of (c) is taken at low pump power of 2.5 mW.

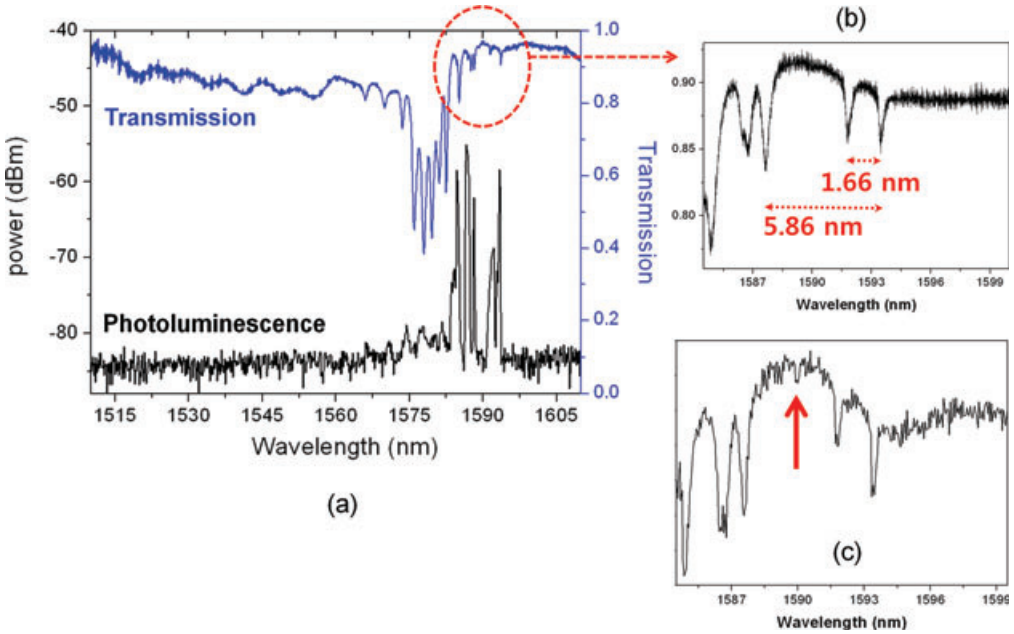

Figure 12 (online color at: www.lpr-journal.org) (a) Transmission and photoluminescence spectra with fiber in contact. (b) Magnified transmission spectrum showing two sharp RPC peaks. (c) Confirmation of the 3rd RPC mode using off-centered microfiber.

ing at 1589.3 nm (Fig. 11b), interference patterns reminiscent of Fabry-Perot resonances are observed in the spectral windows of 1605.5–1680.1 nm and 1525.7–1582.0 nm. Interestingly from the 418-nm sample (Fig. 11c), rich lasing behaviors are observed over a wide spectral range of 1534.4–1542.2 nm even without the microfiber. Among many peaks, the rightmost peak at 1547.6 nm in the red curve is associated with the RPC mode. When the peak pump power is decreased to 2.5 mW, only two rightmost lasing modes at 1542.2 nm and 1547.6 nm survive as shown in the inset of Fig. 11c. The lasing mode at 1542.2 nm is identified as the first guided Fabry-Perot (FP) mode of the bare photonic crystal waveguide. Note that the wavelength difference ($\Delta\lambda = 5.4$ nm) between the RPC mode and the first guided FP mode agrees well with that ($\Delta\lambda = 5.8$ nm) obtained previously by FDTD computation. All the other modes at shorter wavelengths are attributed to the Fabry-Perot resonance of the bare photonic crystal waveguide. Another way of obtaining the reference photoluminescence spectrum is to place the curved microfiber at the end of the photonic crystal waveguide using the same experimental setup. No photonic well can be formed in this case. This photoluminescence spectrum represents the bare photonic crystal waveguide, in contrast to the standard case of RPC modes as shown in Fig. 11.

A straightforward method to identify the resonant mode is traditional transmission measurement. In the current fiber-coupled setup, this can be done easily by inputting a tunable diode laser and sweeping a wavelength around 1.5 μm through one end of the single mode fiber and collecting the transmitted output versus a wavelength on the other end. This transmission experiment is performed for additional confirmation of the RPC mode. To minimize optical absorption effects at the band tail of semiconductor quantum wells, photonic crystal waveguides having TE1-even mode cutoff frequencies smaller than the quantum well transition frequency are fabricated and tested. Even with these samples (smaller material gain) made for the transmission experiment multitudes of laser modes are easily excited with sufficient optical pumping, as shown in the photoluminescence spectrum (black curve) of Fig. 12a. For example, two distinct RPC modes are noticeable below the cutoff frequency.

The transmission data (blue curve) of this reconfigurable resonator are shown in Fig. 12a–c. Observe two rightmost RPC peaks ($\lambda > 1590$ nm) that can be identified in both transmission and photoluminescence spectra, at the same respective spectral positions. In the enlarged transmission spectrum of Fig. 12b, two distinctive resonant modes are clearly identified in the spectral region below the cutoff frequency. The spectral separations between the 1st and 2nd RPCL modes and the 1st RPCL mode and the guided mode are 1.66 nm and 5.86 nm, respectively. These values are in good agreement with FDTD predictions. The third mode is not clearly shown in this Fig. 12b because of the extremely small coupling strength. However, when the fiber is finely displaced in the direction perpendicular to the linear waveguide, the third RPC mode is faintly observable by slightly improving mode-matching conditions, as shown in Fig. 12c. Q-factors of the 1st, 2nd RPC modes and the first waveguide FP mode are measured to be 5800, 4200, and 3900 with the coupling efficiencies of 2.15%, 2.58%, and 4.00%, respectively. Here, all the Q-factors seem to be limited by the remaining absorption tail of quantum wells.

In the transmission spectrum of Fig. 12a, one can see rich traces of photonic crystal guided FP modes in the spectral region of 1560–1583 nm. The pronounced FP dip at 1578.0 nm indicates strong optical coupling between the

microfiber and the finite-size photonic crystal waveguide. In fact, from the transmission spectrum of Fig. 12a, one can construct a dispersion curve of the photonic crystal waveguide mode. Remember that the minimum wave vector interval ($\Delta k_n = a/2L$) of 0.008 in the momentum space is inversely related to the finite length ($L = 61a$) of the photonic crystal waveguide of interest. Then the dispersion curve can be drawn as a simple collection of all the FP resonance points in the transmission spectrum, placed at integer multiples of Δk_n [51, 54, 55]. This Fig. 13 shows that all the FP resonances in the transmission spectrum find their position smoothly on the calculated dispersion curve of the TE1-even photonic crystal waveguide mode above the cutoff frequency. From these analyses, the effective group index (velocity) of the guided mode can also be deduced. The effective group index up to 15 is estimated. In contrast to this observation, the three RPC resonances do not fit to this dispersion curve and find themselves at frequencies well below the cutoff. Therefore, the physics associated with these three new modes should be of different origin than that of the guided mode. These are the reconfigurable photonic crystal resonances created by the contact of the microfiber with the photonic crystal waveguide.

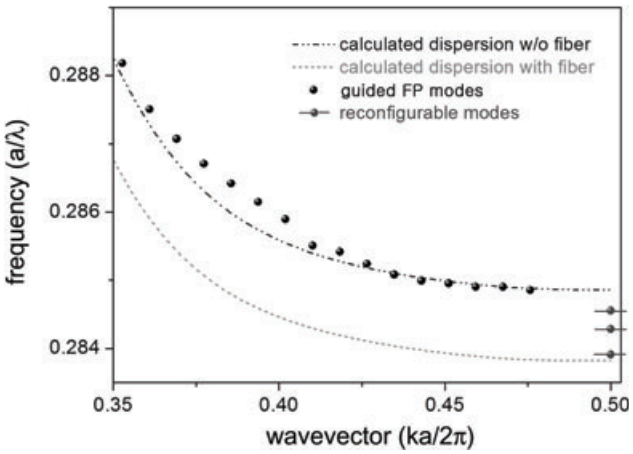

Figure 13 Construction of dispersion curve for photonic crystal waveguide. Dots are constructed from guided FP peaks of measured transmission data, imported from Fig. 12a. Each resonant frequency is equally space by the discrete wave vector interval (Δk_n) of 0.008. Note that three peaks corresponding to the RPC modes are in a class characteristically different from the waveguide mode.

4.2. Two-dimensional relocation of resonant cavity

Square-lattice photonic crystals are fabricated on a 200-nm-thick InGaAsP slab in which four quantum wells exist as an active medium. The size of the pattern is $50 \times 20\,\mu m^2$, which is large enough to provide a room for two dimensional movement. The Fig. 14a shows a scanning electron microscopy (SEM) image of a fabricated square lattice photonic crystal. The lattice constant (a) and the air hole radius (r) were 530 nm and $0.35a$, respectively. A curved microfiber is fabricated by tapering a single mode fiber down to 1.0 μm and bent such that R is $\sim 90\,\mu m$. The sample is loaded on a rotating stage and adjusted until the boundary of the pattern is aligned with the microfiber by looking at the CCD image. The boundary of the square pattern is in the Γ-X direction. Experimentally the microfiber can be aligned better than 2 degrees along the Γ-X direction, in which case the Q-factor degrades less than17%. A 980-nm diode laser is pulse-pumped through one end of the curved microfiber and the photoluminescence from the resonator is collected evanescently using the same microfiber. The width of the pump pulse is 20 ns at a frequency of 1.0 MHz.

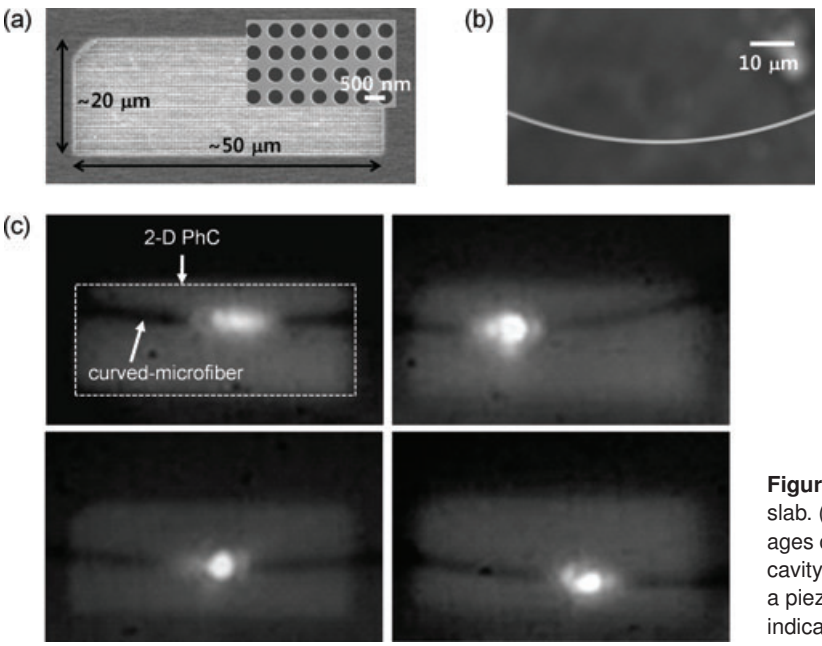

Figure 14 (a) InGaAsP square-lattice photonic crystal slab. (b) Highly-curved microfiber. (c) Infrared CCD images of RPC lasing spots. In-situ relocation of resonant cavity is demonstrated by moving the microfiber using a piezoelectric translator in real time. Dotted rectangle indicates the boundary of photonic crystal pattern.

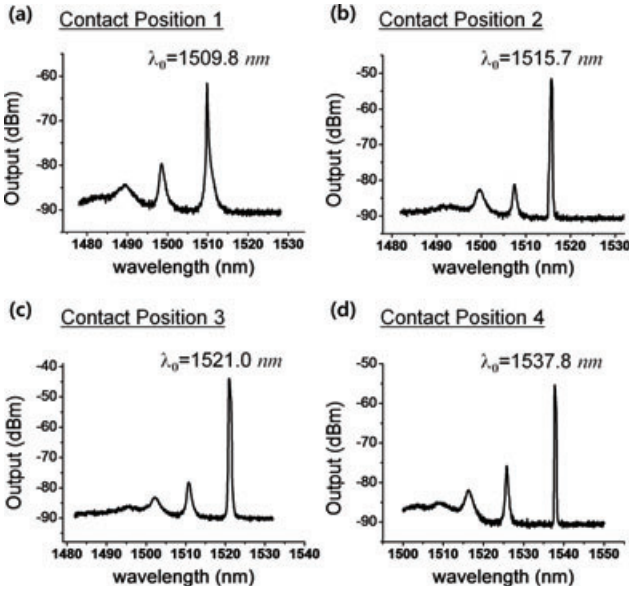

Figure 15 Lasing spectra of 2-D RPC modes when the curved-microfiber contacts on the various points of square lattice PhC slab.

Laser oscillation is observed when the curved microfiber is in contact with the photonic crystal slab and aligned along the Γ-X direction of the square lattice. In contrast, no lasing is observed along the Γ-M direction**.** Repeated lasing is achieved over the patterned area. The lasing wavelength varies (1510–1540 nm) from position to position because of the nonuniformity of the fabricated sample, as showin in Fig. 15. The common feature of these photoluminescence spectra in this figure is that two or three weak resonant peaks appear at wavelength (frequency) shorter (higher) than the strongest peak. The measured $\Delta\lambda_1$ (the gap between 1st and 2nd modes) are 8.3∼ 12.0 nm and $\Delta\lambda_2$ (the gap between 2nd and 3rd modes) are 7.8∼ 9.4 nm. FDTD computations predict 11.3 nm for $\Delta\lambda_1$ and 6.5 nm for $\Delta\lambda_2$. Measured $\Delta\lambda_2$ is slightly larger than the prediction and the discrepancy is ascribed to the experimental variation of the contact condition of the microfiber. The peak lasing threshold pump power is about 650 μW. The large spectral separation between the lasing modes excludes the possibility of band edge lasing and support lasing from microfiber-induced RPC modes [1, 44, 56–58]. In the case of the band edge lasing, the spectral interval between the successive modes is be <0.2 nm estimated by the Fabry-Perot condition of $\Delta k = \pi/L$, where L (50 μm) is the length of the photonic crystal pattern.

The position of the lasing cavity is monitored from the top using an IR CCD camera with a 20× objective lens (N. A. = 0.42) by collecting the scattered laser light. The repeatable re-location of the RPC is tested by detaching and moving the curved microfiber to an arbitrary point on the 50×20-μm^2-wide two-dimensional photonic crystal plane as shown in Fig. 14c. The dotted rectangle in this figure indicates the boundary of the square-lattice photonic crystal pattern. The black curve passing though the pattern is the curved microfiber. The lasing wavelengths also show some spread owing to the variation of the air hole size and the curvature R.

5. Light extraction through microfiber

The tapered optical fiber used for the experiment is fabricated by heating a single-mode fiber with a torch flame and slowly pulling the fiber apart until a micron-size waist region is created [59, 60]. The effective index of microfiber is about 1.2 when the fiber diameter is 1.0 μm [47] and the light coupling with the photonic crystal waveguide mode occurs only for the propagating waves having wave vector components near $k_n = 0.36\ (= k_{n,\text{vacuum}} \times n_{\text{fiber}} \sim 0.3 \times 1.2)$. For the fundamental RPC mode where the radiation components are smoothly suppressed as previously shown in Fig 6b, the total optical loss is dominated mainly by the coupling loss (transmission) into the microfiber. A quite respectable coupling efficiency of ∼ 26% is obtained theoretically for the non-modified W1-waveguide structure. For further enhancement of the out-coupling efficiency, one needs to get ideas in the wave vector space (**k** space) where the real-space RPC mode is transformed into its conjugate *Fourier-transformed* (FT) RPC mode. For efficient photon coupling, the FT RPC mode should have a good overlap with the wave vector components of the microfiber mode. For example, one can increase the width of the FT RPC mode in the **k** space or push the fiber-coupling line closer to the FT RPC mode profile as shown in Fig. 6b.

To widen the extent of the FT RPC mode in the **k** space, one needs to squeeze the size of the RPC mode in the real space. In other words, a narrow photonic well is needed for better photon transfer into the microfiber. The width of photonic well is expressed as $\sqrt{2R \cdot \alpha}$ in Eq. (2) and can be controlled by modifying R and/or α. The decay length α that describes the extent of the evanescent field is determined mainly by the refractive indices of the photonic crystal waveguide and the surrounding dielectric. Therefore, it is nearly independent on the detailed waveguide structure and the diameter of the microfiber. On the other hand, the curvature of the microfiber can be changed rather easily. So, mechanical control of the curvature is a realistic option for in-situ tuning of the photonic well. Figure 16 shows cutoff frequency profiles and energy distributions for two situations with different radii of curvature, 70 μm and 20 μm, respectively. Observe that the resonant mode is laterally confined inside the wavelength-scale Gaussian photonic well.

The coupling efficiency, which is proportional to the ratio of photon density in the microfiber to that in the cavity, increases with the decrease of the radius of curvature. When $R = 20$ μm, the coupling efficiency can be made as large as 80%, with Q-factor and mode volume of 70,000 and $1.9(\lambda/n)^3$, respectively. Figure 17 summarizes the coupling efficiency and Q-factor as a function of the radius of curvature R. Note that the total Q-factor decreases when the coupling efficiency increases. The reduction of the total Q-factor is naturally attributed to the transmission into a microfiber. The near-field intensity profiles at the center

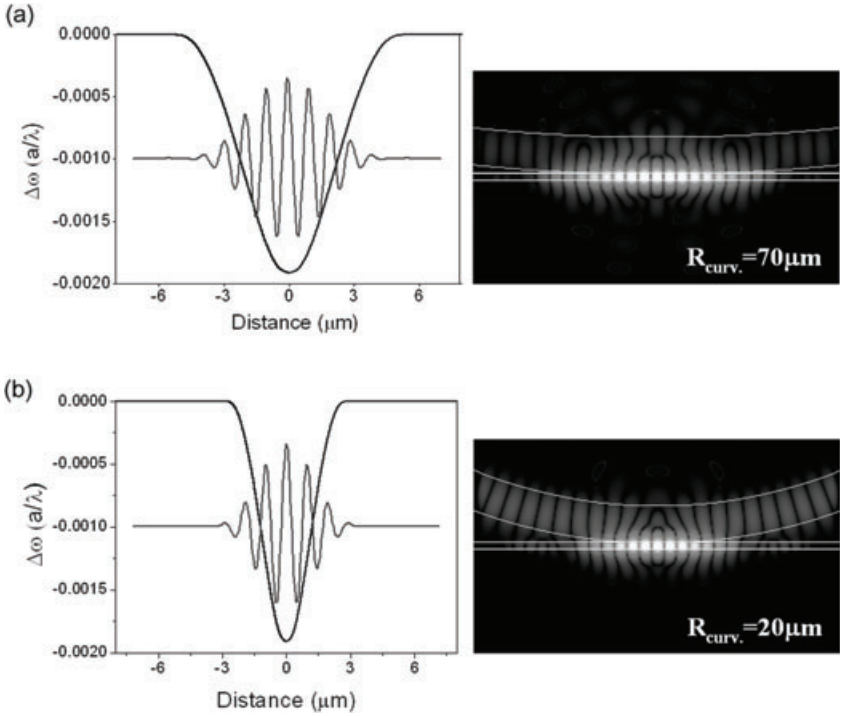

Figure 16 (Left) Photonic well and electric field profiles of 1-D RPC mode with different radii of curvature of microfiber (R_{curv}). (Right) Corresponding intensity profiles in logarithm scale on y-z plane. (a) $R_{curv} = 70\,\mu m$, (b) $R_{curv} = 20\,\mu m$.

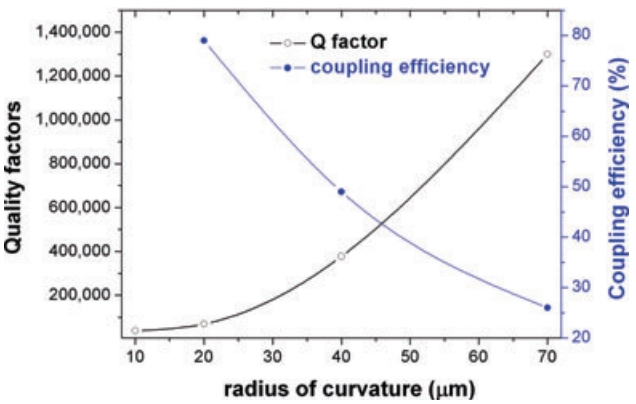

Figure 17 (online color at: www.lpr-journal.org) Effects of curvature variation on the Q-factor and coupling efficiency of the fundamental 1-D RPC mode.

of the slab for different curvatures are also plotted in the right hand side of Fig. 18. The width of the Gaussian profile directly follows that of the photonic well. In practice, the lower bound of the radius of curvature is limited by the fiber's tension and the bending loss. Actually, the smallest radius of curvature experimentally fabricated is 70 μm.

The coupling efficiency can also be controlled, without modifying the fiber shape, by moving the fiber-coupling line closer to the FT RPC resonance in the Fourier-transformed **k** space, as indicated in Fig. 6b. The position of the fiber-coupling line is determined by the two parameters, the effective index of the microfiber and the resonance frequency. Therefore, if one is able to manipulate the resonant frequency, the **k**-space fiber-coupling line can also be moved closer to the FT RPC resonance. The coupling efficiency tends to increase with the normalized frequency. Two methods that induce the increase of the normalized frequency (the reduction of the effective index), without changing the curvature, are tested. One is the increase of the air-hole size nearest to the photonic crystal waveguide (Fig. 19a). For example, when the radius of nearest air-holes increases from $0.30a$ to $0.33a$, the coupling efficiency increases up to 90% with a reduced Q factor ($Q = 54{,}000$). The other way is to introduce an array of the small air-holes along the center of the photonic crystal waveguide (Fig. 19b). As shown in Fig. 19, the coupling efficiency tends to increase with the resonance frequency at the expense of the Q factor. For realistic photon collection, one has to allow a certain amount of optical losses that is unavoidable. However, it is still encouraging that, by a simple touch of the photonic crystal waveguide structure, a high coupling efficiency with a moderately large Q-factor can be realized.

In the case of the 2-D RPC modes, the wave vector is smaller than that of the 1-D RPC mode. Therefore, the phase matching with the low-index silica fiber mode is better satisfied and the higher coupling into the microfiber is expected. A theoretical collection efficiency of 80% ($r = 0.35a$) is obtained from the fundamental RPC mode that has a Q-factor of 25,900.

Table 1 Quality factors (Q), modal volumes (V_{eff}), coupling efficiencies (η) and resonance-gaps ($\Delta\lambda$) for 1-D and 2-D RPC modes. $\Delta\lambda_{(a,b)}$ represents the spectral gap between ath and bth modes. The values in parentheses show the measured data.

RPC mode	Q	V_{eff} $(\lambda/n)^3$	η (%)	$\Delta\lambda_{(1,2)}$ (nm)	$\Delta\lambda_{(2,3)}$ (nm)
1-D RPC	1.3×10^6	2.6	26	1.8 (1.7)	1.7 (1.2)
2-D RPC	2.6×10^4	2.4	80	11.3 (10.2)	6.5 (8.6)

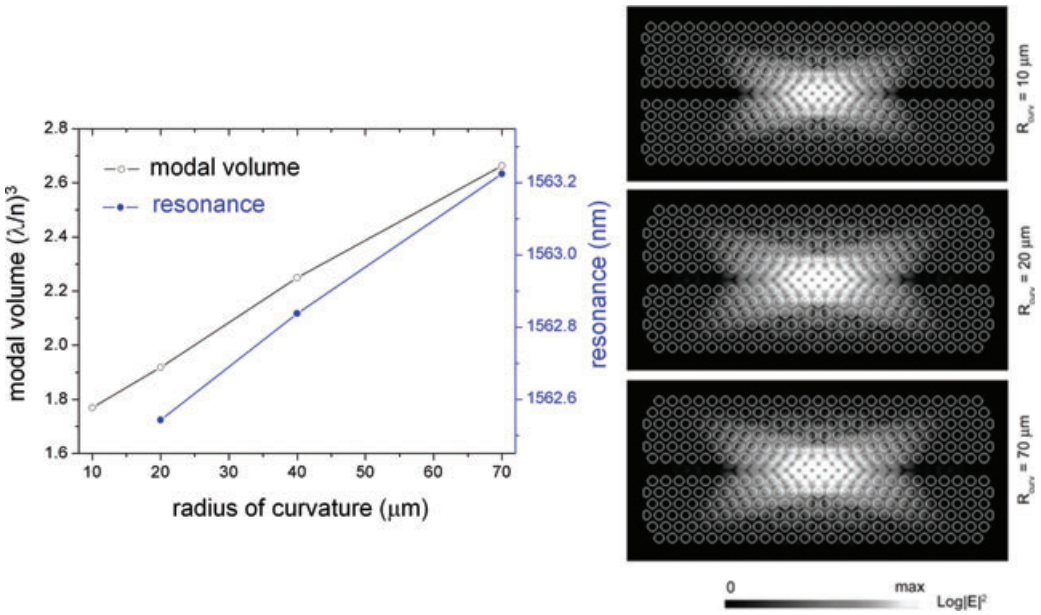

Figure 18 (online color at: www.lpr-journal.org) Curvature-dependent mode volume and resonance wavelength. Right figures show electric field intensity distributions in logarithm scale. $R_{\mathrm{curv}} = 10$, 20, and 70 μm.

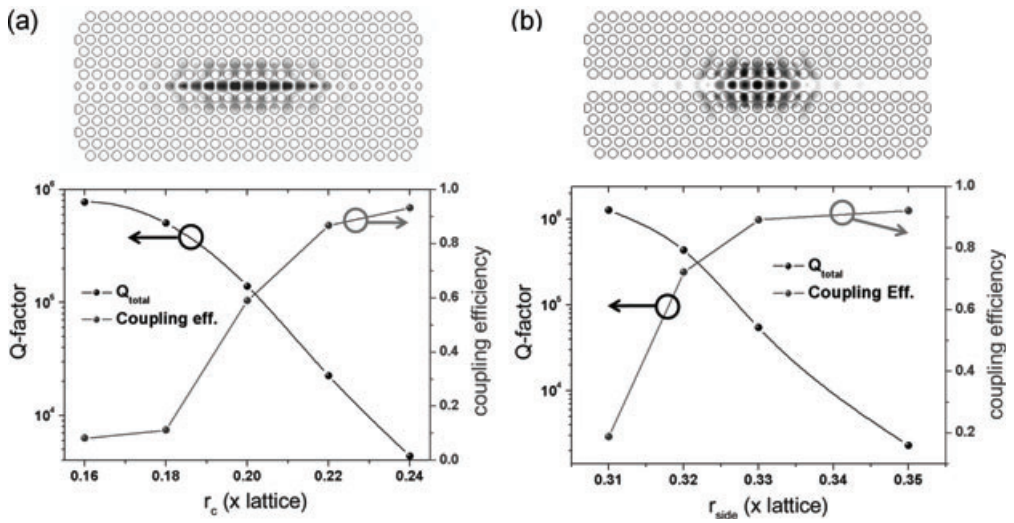

Figure 19 Calculated coupling efficiencies and Q-factors. (a) Dependence on the radius of center air holes, r_c. (b) Dependence on the radius of nearest air holes, r_{side}. Top two images show typical intensity profiles corresponding to (a) and (b), respectively.

6. Spectral tuning of resonances

The spectral tunability is another interesting feature of the microfiber-coupled RPC resonator, in addition to the spatial reconfigurability explained so far. The basic physics is the control of the dimension of the photonic well. One can expect the shift of the resonant frequency under the physical perturbation of the photonic well. Remember that the width of photonic well increases with the product of the radius of curvature of the microfiber (R) and the decay length (α). In the experiment, one can adjust the curvature of microfiber slightly by pushing down or pulling up the microfiber, in a repeatable fashion, as depicted in Fig. 20. As one moves the microfiber toward the slab, the microfiber sticks suddenly to the photonic crystal, once the distance between the two hits a certain lower bound. This static attractive force is believed to be the van der Waals force. As soon as the contact is made, the radius of curvature jumps discretely to a smaller value of 109 μm from 116 μm as shown in Fig. 20b. Once contacted, the microfiber tends to stay there until sufficient vertical pulling force is applied. Therefore, if one applies a not-too-large upward force, the shape and curvature of the microfiber are deformed without being detached, as shown in this figure (c) and (d). The radius of curvature can be adjusted from 109 μm to 105 μm. On the other hand, if one pushes down the microfiber after the contact, the radius of

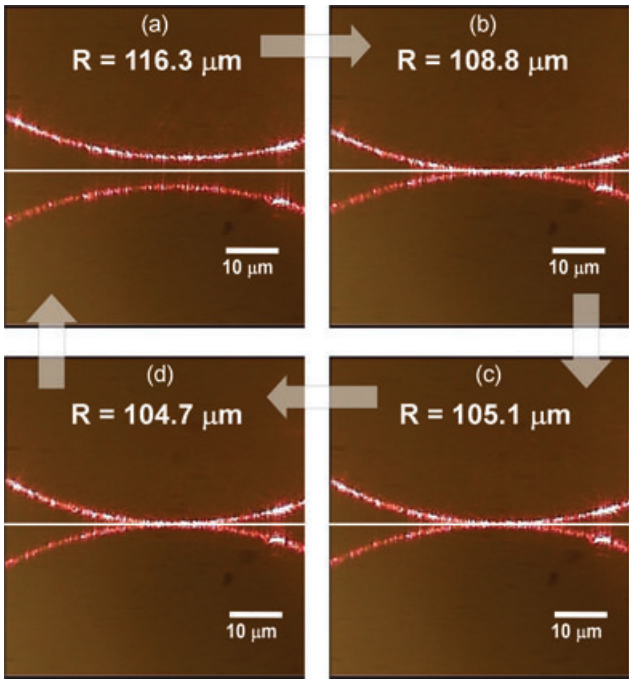

Figure 20 (online color at: www.lpr-journal.org) Images showing deformation of microfiber. Setup of Fig. 9b is used for these pictures.

curvature increases. In this case, however, the microfiber tends to slip away from the initial position when applying the downward force. Pushing down the curved microfiber is not a dependable way of the spectral tuning.

Effect of curvature variation is summarized in Figs. 21 and 22. The radius of curvature is directly related to the size of the reconfigurable cavity and the resonance wavelength is found to increase with the radius of curvature. The tuning range is measured to be 0.57 nm (Fig 22), about 0.03% of the resonance wavelength. In fact, sub-nanometer spectral tuning is easily achieved experimentally. The tuning range is related to the depth of the Gaussian photonic well. Experimental curvature dependence of the resonant wavelength and Q factor is shown in Fig. 21a. The 1st RPC mode at the bottom of the Gaussian photonic potential well experiences the smallest spectral shift. Computationally, when the radius of curvature is varied between 104 μm and 109 μm, the relative spectral shifts of the 1st and 2nd RPC modes are estimated to be 0.01%, 0.03%, respectively (Fig. 21b). In general, for resonant modes originating from the TE1-even photonic crystal waveguide mode, the lower-frequency resonant mode (where the group index is larger) should undergo the smaller spectral shift upon external perturbation. Unlike this expectation, the spectral shift (∼0.57 nm) of the smaller-frequency RPC mode is measured to be larger than that (∼0.42 nm) of the higher-frequency FP mode, as shown in Fig. 22. This is one of the unambiguous evidences that those RPC modes near 1594 nm are characteristically different from the band edge mode.

In the 2-D RPC configuration, the broader spectral tuning is easily achieved. The spectral tuning is measured by adjusting the curvature of the microfiber at a fixed pump

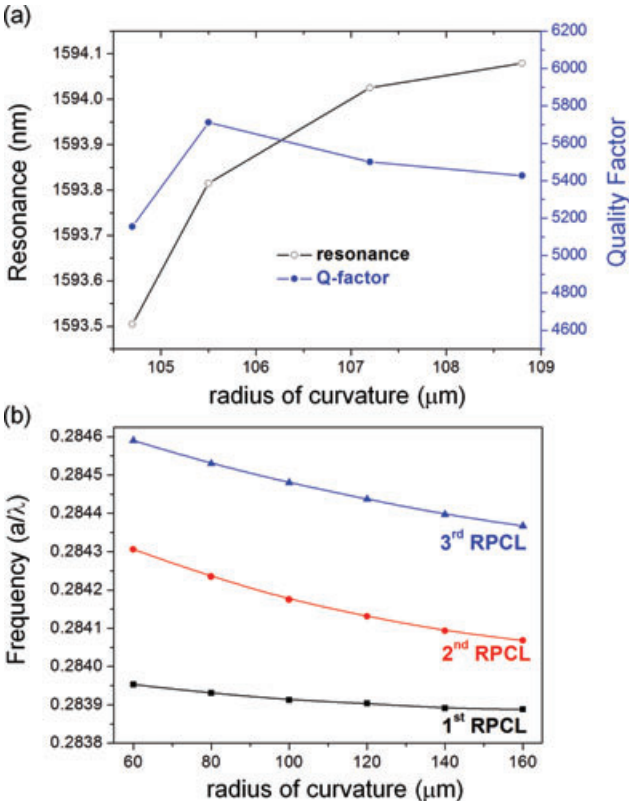

Figure 21 (online color at: www.lpr-journal.org) (a) Effects of curvature variation on resonance wavelengths and Q-factors of measured 1-D RPC modes. (b) Calculated resonant frequencies of 1-D RPC modes.

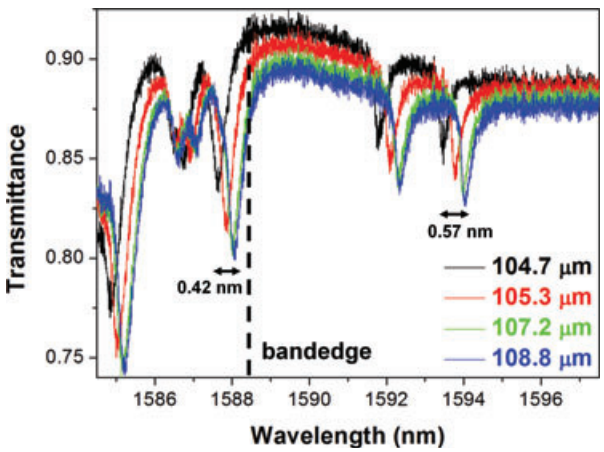

Figure 22 (online color at: www.lpr-journal.org) Spectral tuning of 1-D RPC resonator. Four transmission spectra are taken from one sample by varying the curvature of microfiber.

power of 5 mW as shown in Fig. 23. Actually, lasing spectra are taken by gradually pulling the curved microfiber up, decreasing R. The wavelength of the 1st RPC mode redshifts by 8.4 nm, from 1497.1 to 1505.5 nm. Note that this tuning range is larger than that of the 1-D RPC configuration, by more than an order of magnitude.

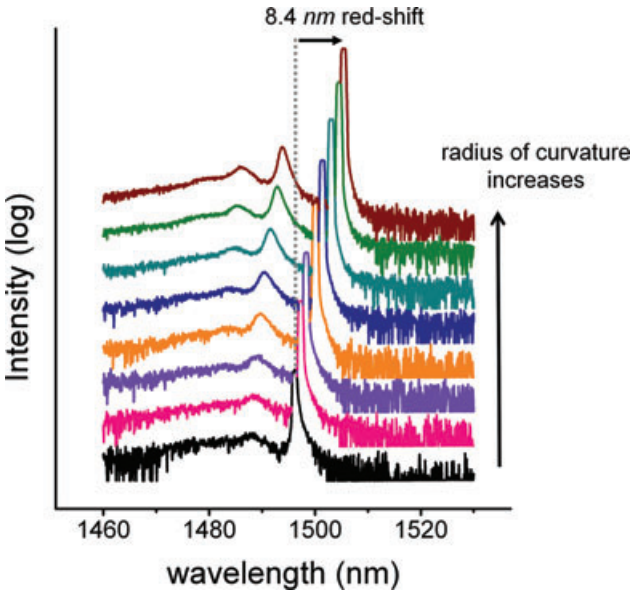

Figure 23 (online color at: www.lpr-journal.org) Spectral tuning of 2-D RPC modes. The lasing wavelength redshifts 8.4 nm, from 1497.1 nm to 1505.5 nm.

7. Summary

Researchers working in nanophotonics have been searching for various means to utilize the strong Purcell effect inherent to wavelength-scale resonators having high Q/V values. Encouraged by the availability of the high-Q semiconductor photonic crystal resonator, the incorporation of a single quantum dot into a high-Q/V cavity has become a realistic experimental option for the solid-state single photon source [61–63]. The challenging task has been the good overlap of two resonances, the quantum dot and the photonic crystal resonance, of different nature. The precise and simultaneous spatial-overlap and spectral-overlap between the cavity resonance and the quantum dot have been dearly sought after [64]. Thanks to the advancement of nanofabrication and coupling techniques, placing a 'right' (resonant frequency) quantum dot at a 'right' place (antinode) have become a realistic experimental task that can be challenged [33, 65]. The on-demand reconfigurable photonic crystal resonator reviewed here is one option that can answer these questions experimentally. The microfiber-coupled RPC resonator is advantageous because it can be defined repeatedly, simply by moving a curved microfiber. The efficient out-coupling into a single mode fiber can also be achieved at the moderate expense of the Q-factor. Moreover, nanometer spectral tuning capability that is available by changing the curvature of the microfiber is a handy option available in the RPC resonator. The reconfigurable photonic crystal resonator enables all three critical requirements (the spatial overlap, the spectral overlap, the efficient out-coupling) at the same time and could be a viable candidate platform for the single photon source. If an artificial atom (quantum dot) can be inserted in a wavelength-scale photonic crystal cavity with authority, one is able to perform cavity quantum electrodynamics experiment using a semiconductor micro-chip. And a new era of semiconductor cavity quantum electrodynamics can be envisioned.

Acknowledgements. This research was supported by the National Research Foundation of Korea (NRF) grant funded by the Korea government (MEST) (No. 2007-0093863), Basic Science Research Program through the National Research Foundation of Korea (NRF) funded by the Ministry of Education, Science and Technology (2009-0087691), and WCU (World Class University) program through the National Research Foundation of Korea funded by the Ministry of Education, Science and Technology (R31-2010-000-10071-0).

Received: 24 August 2010, **Revised:** 3 December 2010, **Accepted:** 11 January 2011

Published online: 14 February 2011

Key words: Photonic crystal, reconfiguration, microresonator, microfiber, tuning.

Myung-Ki Kim received the M. S. and Ph. D. degrees from Korea Advanced Institute of Science and Technology, Daejeon, Korea, in 2005 and 2009, respectively, all in physics. From September to December in 2009, he was a BK-21 researcher in the Department of Mechanical Engineering at Korea Advanced Institute of Science and Technology. Since 2010, he has been a Postdoctoral Fellow in the Department of Electrical Engineering and Computer Sciences at the University of California, Berkeley. His current research interests are plasmonic crystal based nano-devices, photonic crystals, and nano light-emitting diodes. He has authored or co-authored more than 40 journals and conference papers.

Ju-Young Kim received the B. S. and M. S. degrees from KAIST, Daejeon, Korea, in 2005 and 2007, respectively, all in physics. He will receive the Ph. D. degree in physics from KAIST in Jan. 2011. His current research interests are fiber-coupled photonic crystal resonators for cavity QED applications and nanophotonic structures for photonic integrated circuits.

Ju-Hyung Kang received the B. S., M. S. and Ph. D. degrees from Korea Advanced Institute of Science and Technology (KAIST), Daejeon, Korea, in 2005, 2007 and 2010, respectively, all in physics. Since 2010, he has been a Postdoctoral Fellow in the Department of Physics at the Korea University, Korea. His current research interests are surface plasmonic and photonic crystal cavities for high speed light emitting devices, lasers and biochemical applications.

Byeong-Hyeon Ahn received the B. S. degree from KAIST, Daejeon, Korea, in 2007 in physics. He is currently working toward the Ph. D. degree in Department of Physics at KAIST. Since 2010, he has been a National Junior Research Fellow in Korea. His main interest lies on a highly efficient single photon source based on fiber-coupled photonic crystal cavities.

Yong-Hee Lee pioneered and demonstrated the 850-nm proton-implanted top-emitting VCSELs in 1990 during his stay at AT&T Bell Laboratories. In 1991, he joined the Department of Physics in KAIST. In recent years his main interest lies on photonic band gap laser structures and nano-photonic integrated optical circuits. His laboratory demonstrated various forms of 2D photonic band gap lasers from triangular and rectangular lattices. He received the National Academy of Sciences Award in 2002 and the *2003 IEEE LEOS Distinguished Lecturer Award*. He was elected as an *IEEE Fellow* in 2007. He co-authored over 170 papers related to VCSELs and photonic crystals.

References

[1] M. Notomi, K. Yamada, A. Shinya, J. Takahashi, C. Takahashi, and I. Yokohama, Phys. Rev. Lett. **87**, 253902 (2001).
[2] A. Mekis, J. C. Chen, I. Kurland, S. Fan, P. R. Villeneuve, and J. D. Joannopoulos, Phys. Rev. Lett. **77**, 3787–3790 (1996).
[3] S. G. Johnson, P. R. Villeneuve, S. Fan, and J. D. Joannopoulos, Phys. Rev. B **62**, 8212–8222 (2000).
[4] M. Notomi, A. Shinya, S. Mitsugi, E. Kuramochi, and H. Ryu, Opt. Express, **12**(8), 1551–1561 (2004).
[5] S. F. Mingaleev and Y. S. Kivshar, JOSA B **19**(9), 2241–2249 (2002).
[6] Y. Akahane, T. Asano, B.-S. Song, and S. Noda, Nature **425**, 944–947 (2003).
[7] B.-S. Song, S. Noda, T. Asano, and Y. Akahane, Nature Materials **4**, 207–210 (2005).
[8] T. Yoshie, J. Vučković, A. Scherer, H. Chen, and D. Deppe, Appl. Phys. Lett. **79**, 4289 (2001).
[9] K. Srinivasan and O. Painter, Opt. Express **10**(15), 670–684 (2002).
[10] E. Kuramochi, M. Notomi, S. Mitsugi, A. Shinya, T. Tanabe, and T. Watanabe, Appl. Phys. Lett. **88**, 041112 (2006).
[11] K. Srinivasan, P. E. Barclay, O. Painter, J. Chen, A. Y. Cho, and C. Gmachl, Appl. Phys. Lett. **83**, 1915 (2003).
[12] P. B. Deotare, M. W. McCutcheon, I. W. Frank, M. Khan, and M. Lončar, Appl. Phys. Lett. **94**, 121106 (2009).
[13] H.-G. Park, S.-H. Kim, S.-H. Kwon, Y.-G. Ju, J.-K. Yang, J.-H. Baek, S.-B. Kim, and Y.-H. Lee, Science **305**, 1444–1447 (2004).
[14] O. Painter, R. K. Lee, A. Scherer, A. Yariv, J. D. O'Brien, P. D. Dapkus, and I. Kim, Science **284**, 1819–1821 (1999).
[15] S. Noda, M. Yokoyama, M. Imada, A. Chutinan, and M. Mochizuki, Science **293**, 1123–1125 (2001).
[16] A. A. Erchak, D. J. Ripin, S. Fan, P. Rakich, J. D. Joannopoulos, E. P. Ippen, G. S. Petrich, and L. A. Kolodziejski, Appl. Phys. Lett. **78**, 563 (2001).
[17] M. Boroditsky, T. F. Krauss, R. Coccioli, R. Vrijen, R. Bhat, and E. Yablonovitch, Appl. Phys. Lett. **75**, 1036 (1999).
[18] J. J. Wierer, M. R. Krames, J. E. Epler, N. F. Gardner, M. G. Craford, J. R. Wendt, J. A. Simmons, and M. M. Sigalas, Appl. Phys. Lett. **84**, 3885 (2004).
[19] T. N. Oder, K. H. Kim, J. Y. Lin, and H. X. Jiang, Appl. Phys. Lett. **84**, 466 (2004).
[20] D.-H. Kim, C.-O. Cho, Y.-G. Roh, H. Jeon, Y. S. Park, J. Cho, J. S. Im, C. Sone, Y. Park, W. J. Choi, and Q.-H. Park, Appl. Phys. Lett. **87**, 203508 (2005).
[21] S. McNab, N. Moll, and Y. Vlasov, Opt. Express **11**(22), 2927–2939 (2003).
[22] W. Bogaerts, D. Taillaert, B. Luyssaert, P. Dumon, J. Van Campenhout, P. Bienstman, D. Van Thourhout, R. Baets, V. Wiaux, and S. Beckx, Opt. Express **12**(8), 1583–1591 (2004).
[23] Y. A. Vlasov, X.-Z. Bo, J. C. Sturm, and D. J. Norris, Nature **414**, 289–293 (2001).
[24] H. Kosaka, T. Kawashima, A. Tomita, M. Notomi, T. Tamamura, T. Sato, and S. Kawakami, Appl. Phys. Lett. **74**, 1370 (1999).
[25] M. W. Lee, C. Grillet, C. L. C. Smith, D. J. Moss, B. J. Eggleton, D. Freeman, B. Luther-Davies, S. Madden, A. Rode, Y. Ruan, and Y. H. Lee, Opt. Express **15**(3), 1277–1285 (2007).
[26] H. M. H. Chong and R. M. De La Rue, IEEE Phon. Tech. Lett. **16**(6), 1528–1530 (2004).
[27] J. Zhou, C. Q. Sun, K. Pita, Y. L. Lam, Y. Zhou, S. L. Ng, C. H. Kam, L. T. Li, and Z. L. Gui, Appl. Phys. Lett. **78**, 661 (2001).
[28] B. Wild, R. Ferrini, R. Houdré, M. Mulot, S. Anand, and C. J. M. Smith, Appl. Phys. Lett. **84**, 846 (2004).
[29] M. W. Lee, C. Grillet, S. T. Hanic, E. C. Mägi, D. J. Moss, B. J. Eggleton, X. Gai, S. Madden, D.-Y. Choi, D. A. P. Bulla, and B. L. Davies, Opt. Lett. **34**(23), 3671–3673 (2009).
[30] G. C. DeSalvo, C. A. Bozada, J. L. Ebel, D. C. Look, J. P. Barette, C. L. A. Cerny, R. W. Dettmer, J. K. Gillespie, C. K. Havasy, T. J. Jenkins, K. Nakano, C. I. Pettiford, T. K. Quach, J. S. Sewell, and G. D. Via, J. Electrochem. Soc. **143**, 3652 (1996).
[31] A. Badolato, K. Hennessy, M. Atatüre, J. Dreiser, E. Hu, P. M. Petroff, and A. Imamolu, Science **308**, 1158–1161 (2005).
[32] W. Park and J. B. Lee, Appl. Phys. Lett. **85**, 4845–4847 (2004).
[33] C. Grillet, C. Monat, C. L. C. Smith, B. J. Eggleton, D. J. Moss, S. Frédérick, D. Dalacu, P. J. Poole, J. Lapointe, G. Aers, and R. L. Williams, Opt. Express **15**(3), 1267–1276 (2007).
[34] K. Busch and S. John, Phys. Rev. Lett. **83**, 967–970 (1999).
[35] B. Maune, M. Loncar, J. Witzens, M. Hochberg, T. Baehr-Jones, D. Psaltis, A. Scherer, and Y. M. Qiu, Appl. Phys. Lett. **85**, 360–362 (2004).
[36] C. Schuller, F. Klopf, J. P. Reithmaier, M. Kamp, and A. Forchel, Appl. Phys. Lett. **82**, 2767–2769 (2003).
[37] P. Domachuk, H. C. Nguyen, B. J. Eggleton, M. Straub, and M. Gu, Appl. Phys. Lett. **84**, 1838 (2004).

[38] C. L. C. Smith, D. K. C. Wu, M. W. Lee, C. Monat, S. Tomljenovic-Hanic, C. Grillet, B. J. Eggleton, D. Freeman, Y. Ruan, S. Madden, B. Luther-Davies, H. Giessen, and Y. H. Lee, Appl. Phys. Lett. **91**, 121103 (2007).
[39] D. Erickson, T. Rockwood, T. Emery, A. Scherer, and D. Psaltis, Opt. Lett. **31**(1), 59–61 (2006).
[40] C. Grillet, C. Monat, C. L. Smith, M. W. Lee, S. Tomljenovic-Hanic, C. Karnutsch, and B. J. Eggleton, Laser Photon. Rev. **4**(2), 192–204 (2010).
[41] S. Vignolini, F. Intonti, F. Riboli, D. S. Wiersma, L. Balet, L. H. Li, M. Francardi, A. Gerardino, A. Fiore, and M. Gurioli, Appl. Phys. Lett. **94**(16), 163102 (2009).
[42] B. Cluzell, L. Lalouat, P. Velha, E. Picard, D. Peyrade, J.-C. Rodier, T. Charvolin, P. Lalanne, F. Fornel, and E. Hadji, Opt. Express **16**(1), 279–286 (2008).
[43] C. L. Smith, U. Bog, S. T. Hanic, M. W. Lee, D. K. Wu, L. O'Faolain, C. Monat, C. Grillet, T. F. Krauss, C. Karnutsch, R. C. McPhedran, and B. J. Eggleton, Opt. Express **16**(20), 15887–15896 (2008).
[44] M.-K. Kim, I.-K. Hwang, M.-K. Seo, and Y.-H. Lee, Opt. Express **15**(25), 17241–17247 (2007).
[45] J.-Y. Kim, M.-K. Kim, M.-K. Seo, S.-H. Kwon, J.-H. Shin, and Y.-H. Lee, Opt. Express **17**(15), 13009–13016 (2009).
[46] J. D. Joannopoulos, R. D. Meade, and J. N. Winn, Photonic Crystal (Princeton University Press, Princeton, NJ, 1995).
[47] I.-K. Hwang, G.-H. Kim, and Y.-H. Lee, IEEE J. Quantum Electron. **42**, 131 (2006).
[48] S. G. Johnson, S. Fan, P. R. Villeneuve, and J. D. Joannopoulos, Phys. Rev. B **60**, 5751–5758 (1999).
[49] S. T. Hanic, C. Sterke, M. Steel, B. Eggleton, Y. Tanaka, and S. Noda, Opt. Express, **15**, 17248 (2007).
[50] P. Dirac, The Principles of Quantum Mechanics (Oxford University Press, USA, 1981).
[51] S.-H. Kim, G.-H. Kim, S.-K. Kim, H.-G. Park, Y.-H. Lee, and S.-B. Kim, J. Appl. Phys. **95**, 411 (2004).
[52] I.-K. Hwang, S.-K. Kim, J.-K. Yang, S.-H. Kim, S. H. Lee, and Y.-H. Lee, Appl. Phys. Lett. **87**, 131107 (2005).
[53] G.-H. Kim and Y.-H. Lee, J. Opt. Soc. Korea **7**, 38–41 (2003).
[54] X. Letartre, C. Seassal, C. Grillet, P. Rojo-Romeo, P. Viktorovitch, M. Le Vassor d'Yerville, D. Cassagne, and C. Jouanin, Appl. Phys. Lett. **79**(15), 2312–2314 (2001).
[55] M. W. Lee, C. Grillet, C. G. Poulton, C. Monat, C. L. Smith, E. Mägi, D. Freeman, S. Madden, B. L. Davies, and B. J. Eggleton, Opt. Express **16**(18), 13800–13808 (2008).
[56] S.-H. Kwon, H.-Y. Ryu, G.-H. Kim, and Y.-H. Lee, Appl. Phys. Lett. **83**, 3870–3872 (2003).
[57] K. Kiyota, T. Kise, N. Yokouchi, T. Ide, and T. Baba, Appl. Phys. Lett. **88**, 201904 (2006).
[58] H.-Y. Ryu, S.-H. Kim, S.-H. Kwon, H.-G. Park, and Y.-H. Lee, J. Opt. Soc. Korea **6**, 59–71 (2002).
[59] J. Knight, G. Cheung, F. Jacques, and T. Birks, Opt. Lett. **22**, 1129 (1997).
[60] T. Birks and Y. Li, J. Lightwave Technol. **10**, 432 (1992).
[61] T. Yoshie, A. Scherer, J. Hendrickson, G. Khitrova, H. M. Gibbs, G. Rupper, C. Ell, O. B. Shchekin, and D. G. Deppe, Nature **432**, 200–203 (2004).
[62] D. Englund, D. Fattal, E. Waks, G. Solomon, B. Zhang, T. Nakaoka, Y. Arakawa, Y. Yamamoto, and J. Vučković, Phys. Rev. Lett. **95**, 013904 (2005).
[63] W.-H. Chang, W.-Y. Chen, H.-S. Chang, T.-P. Hsieh, J.-I. Chyi, and T.-M. Hsu, Phys. Rev. Lett. **96**, 117401 (2006).
[64] E. Moreau, I. Robert, L. Manin, V. Thierry-Mieg, J. M. Gérard, and I. Abram, , Phys. Rev. Lett. **87**, 183601 (2001).
[65] K. Srinivasan, O. Painter, A. Stintz, and S. Krishna, Appl. Phys. Lett. **91**(9), 091102 (2007).